Phases and properties of nanocomposites of hydrogen-bonded liquid crystals and carbon nanotubes

M. Petrov,[1,*] B. Katranchev,[1] P. M. Rafailov,[1] H. Naradikian,[1] U. Dettlaff-Weglikowska,[2] E. Keskinova,[1] and T. Spassov[3]
[1]*Institute of Solid State Physics, Bulgarian Academy of Sciences, 72 Tzarigradsko Chaussee Boulevard, 1784 Sofia, Bulgaria*
[2]*School of Electrical Engineering, Korea University, Anam-Dong, Sungbuk-Gu, 136-713 Seoul, Korea*
[3]*Faculty of Chemistry and Pharmacy, University of Sofia "St. Kl. Ohridski," 1 James Bourchier Boulevard, 1164 Sofia, Bulgaria*
(Received 20 June 2012; revised manuscript received 25 April 2013; published 11 October 2013)

We investigated a series of nanocomposites, built of the hydrogen-bonded liquid crystal (LC) *p-n*-heptyloxybenzoic acid (7OBA) and single-walled carbon nanotubes (SWCNTs) by optical microtexture analysis and other complementary methods. The surface orientation strength of the LC cell and the bulk interaction of the dimeric LC molecules with the SWCNTs turn out to mainly govern the type (symmetry), thermal stability, and chirality of the LC states induced in these nanocomposites. As a result, a cascade of phase transitions and phases not typical for pristine 7OBA were observed and additionally confirmed by temperature-dependent Raman spectroscopy and differential scanning calorimetry. The most effective SWCNT concentrations in the LC matrix, ensuring both the necessary conformability between these materials and induction of liquid crystal phases with unique optical and electro-optical properties, were found to be in the range of 0.01–0.007 wt %. Reversal of smectic phases into reentrant nematic states as well as induction of chirality in all LC phases were observed in the SWCNT-7OBA nanocomposite, even though pure 7OBA is typically achiral. However, our most intriguing result is the detection below the reentrant nematic of a triclinic smectic-C_G phase, which is chiral and biaxial, and exhibits bulk ferroelectricity.

DOI: 10.1103/PhysRevE.88.042503 PACS number(s): 61.30.Eb, 61.30.Hn, 73.63.Fg

I. INTRODUCTION

Mixtures of liquid crystals (LCs) with some nonmesogenic nanostructured materials yield promising nanocomposites, able to create a new trend in the LC display techniques [1–16] The concentration of the nonmesogenic component, its homogeneity, and its compatibility with the liquid crystal are of particular significance for the structural, optical, and electrical properties of the nanocomposite. In this sense, single-walled carbon nanotubes (SWCNTs) are the subject of intense research due to their unique anisotropic mechanical, thermal, and electro-optical properties [1,14–20]. Dispersion of SWCNTs in nematic LCs (NLCs) as well as in ferroelectric LCs was applied to create a suitable nanocomposite for low-threshold voltage and faster switching time [14,17]. These improvements in the electro-optical behavior of such nanocomposites are due to trapping by the nanotubes of impurity ions [17], which decreases the dielectric losses [21], as well as to an enhancement of the dielectric anisotropy and the rotational viscosity, and to a conductivity decrease in the nanocomposite [11,14,17]. Furthermore, it has been shown that the self-organization phenomena in the LCs can orient the SWCNTs in the bulk as well as on the surface, especially if an orienting surface is applied in the LC cell [1,2]. The SWCNTs embedded in the LC matrix could also affect the structure of the constituent LC molecules. This is particularly important when these molecules are dimers, and especially dimers formed by linear hydrogen bonding (H bonding). In the latter case, the interaction with the nonmesogenic component in the nanocomposite could provoke a conformation of the LC molecules from closed dimers to opened dimers and monomers or bent dimers which may lead to new electrical and thermal properties, including new phases. Recently, a smectic-*G* phase was induced through intermolecular H bonding between mesogenic *p-n*-alkyloxybenzoic acids (*n*OBA, *n* being the homolog number) and nonmesogenic *p*-aminobenzonitrile [22].

The closed dimers can be viewed also as flexible bent-core-like molecules, showing similarities with phases found in large-size bananalike systems [23–25]. A close similarity was suggested between the smectic-*X* phase found in these substances and the C_G phase or its analog B_7 phase in bent-core liquid crystals [26]. These phases are examples of the typical smectic states where left- and right-handed helices are induced [27,28] in an LC system whose constituent molecules are achiral.

The smectic-C_G phase was predicted long ago by de Gennes and Prost [29]. Being biaxial and fluid in the layers and having a macroscopic hand due to its structure, this phase is a natural candidate to demonstrate induced helices in a system composed of achiral molecules. Since the layer normal $\boldsymbol{N}$ defines a direction independent on the normal to the molecular plane and the molecular polar axis, a large variety of mesophases with different symmetries may result (see Ref. [30] for more details on bent-core molecules). The predicted C_G is interesting because it is characterized by two tilt directions with respect to the layer normal: a tilt of the molecular plane (clinic) and a tilt of the molecular kink direction (leaning). As a result, each smectic layer has a polarization component normal to the layer and the symmetry of the structure is lowered to C_1—a triclinic symmetry in a bulk smectic-LC system [27,28,30–34].

The classical LC *p-n*-alkyloxybenzoic acid is a basic component in forming supramolecular systems. Even without complementary nonmesogenic molecules it displays a supramolecular state [35] due to the dimeric form of its molecule, and its donor ability at contact with a nonmesogen substance predicts rich mesomorphic states. On the other hand, as an achiral LC system, its dimeric structure makes it possible to create an induced chirality, i.e., it is a hopeful candidate for

*Corresponding author: mpetrov@issp.bas.bg

the realization of the long-sought-after C_1 symmetry in LC systems such as the bent-core molecules.

In the present work we prepare mixtures (nanocomposites) of the seventh homolog of *n*OBA with SWCNTs in different concentrations. We explore conditions for thermal stability, compatibility of the SWCNTs with the LC matrix, chirality, and phase transitions and find a series of alternative phases in these nanocomposites. Especially, we provide an example of a smectic-C_G state induced in a low-molecular system such as this nanocomposite. The impact of the surface orientation on the phase formation as well as the mechanism of interaction between the 7OBA molecules and the SWCNTs is discussed.

II. EXPERIMENTAL PROCEDURES

The experiments have been carried out on nanocomposites of the liquid crystal *p*-*n*-heptyloxybenzoic acid (7OBA) with single-walled carbon nanotubes: SWCNT-7OBA. The LC phases of 7OBA comprise a nematic (N) and a smectic-C (S_C) phase. Above N an isotropic (I) state establishes at 146 °C, while the S_C turns into a solid crystal (Cry) state at 92 °C. The $N \rightarrow S_C$ transition takes place at 98 °C. The chemical structure of the *n*OBA molecule is peculiar, as it contains dimers closed by hydrogen bonding as illustrated below for 7OBA:

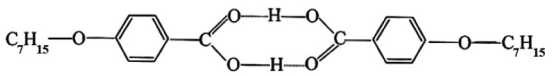

Under bulk or surface influence from outside the closed dimers may transform into open dimers or monomers by breaking of one or both linear H bonds, respectively. Open dimers can further undergo bending at the unbroken H bond, thus adopting a shape similar to the bent-core banana molecules [23–26]. The degree of bending is quantified by the so-called kink vector $\boldsymbol{m} \sim \boldsymbol{n_1} \times \boldsymbol{n_2}$, where $\boldsymbol{n_1}$ and $\boldsymbol{n_2}$ are the unit vectors pointing along the two wings of the dimer.

Here we introduce doping with SWCNTs as a type of external influence by nonmesogenic particles on the 7OBA matrix. We expect a transformation impact of the SWCNTs on both the dimer ring and the molecular chains leading to transformation into bent dimers.

Purified SWCNTs with diameters in the range 1.2–1.4 nm and an aspect ratio of 20–2000, assembled in thin bundles of >2 μm length, produced by arc discharge at Hanwha NanoTech Co., Ltd., were used as purchased. For preparation of a composite 0.6-mg SWCNT, powder was mixed in a mortar with 620 mg of 7OBA during heating. At temperature above 150 °C a dense slurry was formed. The mixing process was continued for 90 min while the temperature of the slurry slowly decreased to 140 °C and the mixture changed from liquid to solid. The final product was a homogeneous gray powder. The SWCNT-7OBA nanocomposites used in the present study were obtained by adding pure 7OBA to this powder. They were examined for their possible LC states at different SWCNT concentrations, cell thickness, and surface orientation.

To create an orienting surface of the LC cell the glass substrates were coated with indium tin oxide (ITO) and subsequently rubbed with a suitable cloth to create unidirectional orientation, i.e., to promote an "easy" axis leading to surface energy minimization. Thus prepared glasses were used as cell walls.

The prepared nanocomposites with different SWCNT concentration c were filled (in the isotropic phase) into the LC cell using capillary forces. The LC cell thickness d was maintained with Mylar spacers to be 8–50 μm, respectively. The temperature T of the sample was varied at a rate of 0.2 °C min^{-1} by a hot stage temperature controller Linkam TMS 90, and was stabilized with an accuracy of ± 0.1 °C. Monitoring of the optical textures was carried out in the xy plane of the LC cell using a video camera (Hitachi) on a microscope (Zeiss NU2). All observations were made in crossed polarizers.

Examination with differential scanning calorimetry (DSC) was performed in inert atmosphere on a PerkinElmer DSC-7 instrument. Comparative DSC scans were recorded for pristine 7OBA and the SWCNT-7OBA nanocomposite between 60 °C and 150 °C.

For the electric-field experiments we used an "up view" geometry, where the electric field was applied along the cell surface normal. A function generator with dc power supply was used in the ac and dc field experiments.

The Raman spectra were measured in backscattering geometry on a HORIBA Jobin Yvon Labram HR visible spectrometer equipped with a Peltier-cooled charge-coupled device (CCD) detector. The 633-nm line of an He-Ne-laser was used for excitation, the absolute accuracy being 0.5 cm^{-1}. The laser beam was focused on a spot of about 10 μm in diameter using microscope optics. The peak frequencies were determined using neon calibration lines by least-squares fit to Voigt profiles.

III. RESULTS AND DISCUSSION

A. Temperature-dependent microtexture analysis

1. Nonoriented LC cells

We started with a commonly used [17] SWCNT concentration, $c = 0.01$ wt % with $d = 20$ μm. We observed the following phase transitions in the nanocomposite: The $I \rightarrow N$ transition takes place at 142 °C (4 °C below the pristine-7OBA value); at 93 °C the transition from N to achiral smectic-C (S_C) is seen [Fig. 1(a)]. At 86 °C a transition from S_C to a reentrant nematic (N_r) phase starts [Fig. 1(b)], and at 81 °C a transition from the N_r to a low-temperature smectic-G phase [Fig. 1(c)] is reached. Finally, at 75 °C a paramorphic solid Cry phase forms.

A richer variety of phases is observed for the same concentration, but in a thinner layer ($d = 8$ μm). After briefly crossing the conventional N phase in an interval of $\approx$1 °C, the nanocomposite forms a chiral nematic phase (N^*) at 142 °C. Then the system enters at 93 °C into a chiral smectic-C ($S_C{}^*$) phase [in Fig. 2(a) the transition $N^* \rightarrow S_C{}^*$ is depicted]. The textures of N^* and $S_C{}^*$ are characterized by typical stripes indicating the helix direction, which in this case lies in the xy cell plane or is tilted with respect to it. Upon further cooling, at 90 °C a reentrant chiral nematic ($N_r{}^*$) phase is reached. Fig. 2(b) presents the $N_r{}^*$ texture. At 86 °C we observe a transition from $N_r{}^*$ to a low-temperature smectic phase [Fig. 2(c)], which is fluid (well indicated by small

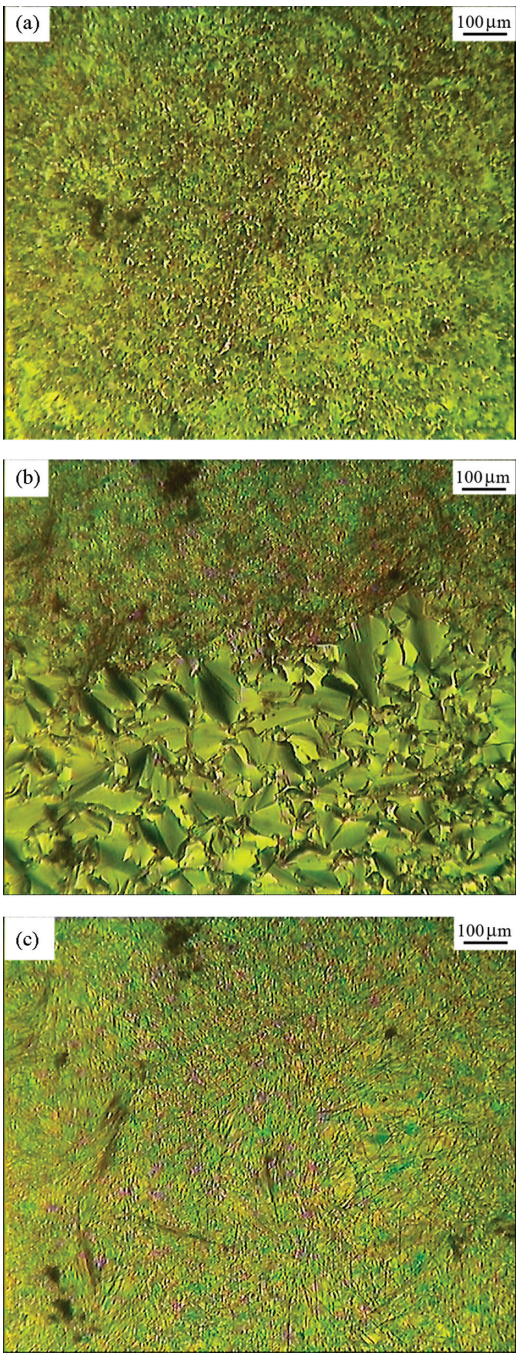

FIG. 1. (Color online) SWCNT-7OBA textures ($c = 0.01$ wt %) undergoing phase transitions in a nonoriented LC cell with $d = 20$ μm: (a) Transition from N to achiral S_C at $T = 93\,^{\circ}$C; (b) transition $S_C \rightarrow N_r$ at $T = 86\,^{\circ}$C (the transition front passing through the middle of the image is clearly seen); (c) transition from N_r to a low-temperature smectic-G phase at $T = 81\,^{\circ}$C.

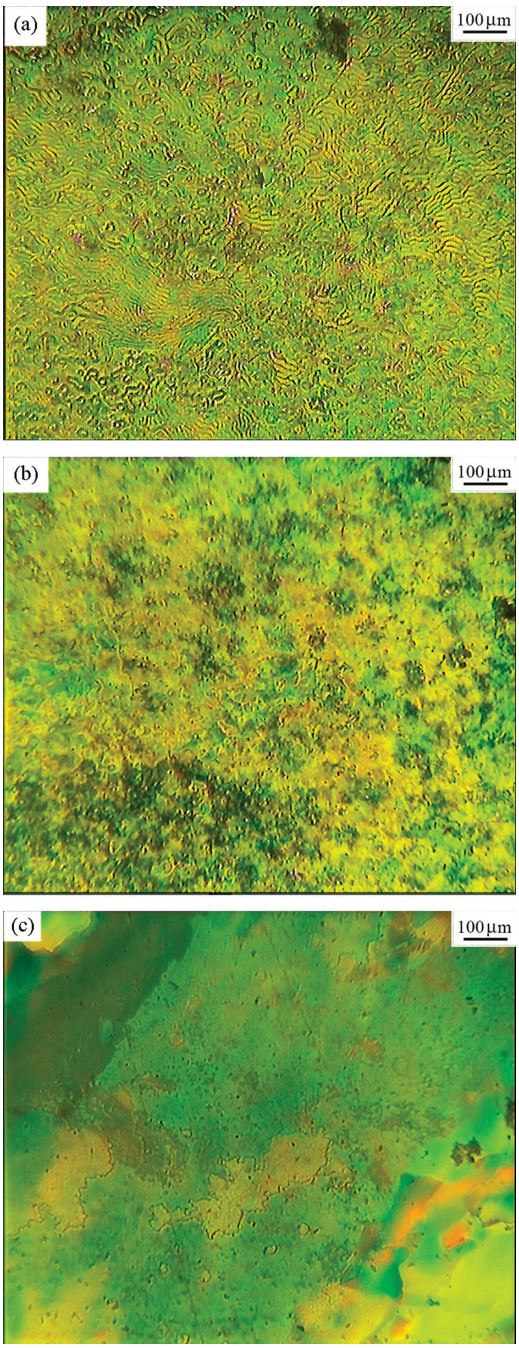

FIG. 2. (Color online) SWCNT-7OBA textures ($c = 0.01$ wt %) in a nonoriented LC cell with $d = 8$ μm: (a) Phase transition from N^* to $S_C{}^*$ at $T = 93\,^{\circ}$C; (b) reentrant $N_r{}^*$ phase at $T = 89\,^{\circ}$C; (c) low-temperature smectic-C_G phase at $T = 86\,^{\circ}$C.

colored glass particles), not smooth, and colored in red and green mosaic domains, thus closely resembling the C_G phase. At very slow cooling ($0.1\,^{\circ}$C min^{-1}) starting from the I phase, the domains grow as fractal nuclei and coalesce into large areas with opposite optical rotation (distinct circular dichroism).

Investigating this low-temperature smectic phase we observe that upon sample rotation in either direction, the red color turns into green and vice versa. Besides this variable birefringence (red and green colors), on entering this phase from the $N_r{}^*$ one we also observe a change in fluidity and the texture loses its smoothness appearing as a colored mosaic texture with equal left- and right-handed helices. This unambiguously shows that this phase is chiral and biaxial. Note that conventional cholesterics and chiral smectic-C^* exhibit no change in color nor in intensity of the transmitted light upon rotating the film between crossed polarizers as they are optically uniaxial. Thus this low-temperature LC phase is identified as a biaxial chiral smectic-C_G phase. The properties

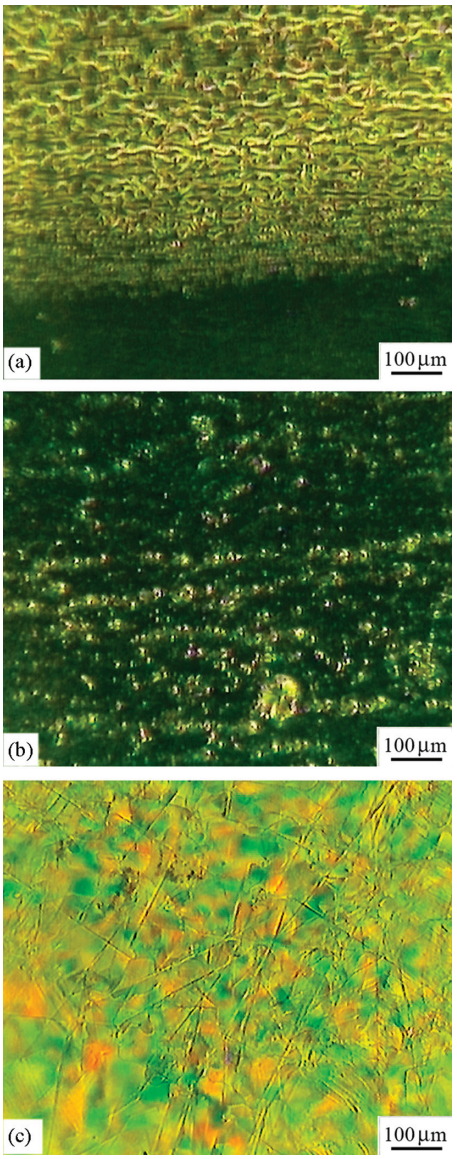

FIG. 3. (Color online) SWCNT-7OBA textures ($c = 0.01$ wt %) in unidirectionally oriented LC cell with $d = 20$ μm: (a) Phase transition $N^* \rightarrow S_C^*$ at $T = 95\,^\circ$C; (b) N_r^* phase at $T = 91\,^\circ$C; (c) C_G phase at $T = 87\,^\circ$C.

of this phase imply a drastic symmetry breaking of the constituent LC molecules. Differently from the conventional S_C phase of pristine 7OBA where the open dimers can only undergo twisting, the observed combination of chirality and biaxiality implies a loss of the linear shape of the LC molecules, i.e., formation of a bent-dimer shape.

2. *Unidirectionally oriented LC cells*

At $d = 20$ μm and $c = 0.01$ wt % we observe a transition to a chiral nematic phase N^* at 142 °C again via brief passing through N. Further, the same sequence of chiral phases proceeds down to smectic-C_G as described for the thinner nonoriented cell with $d = 8$ μm. The $N^* \rightarrow S_C^*$ transition at 95 °C is displayed in Fig. 3(a). Figures 3(b) and 3(c) show the N_r^* and the smectic-C_G texture, respectively.

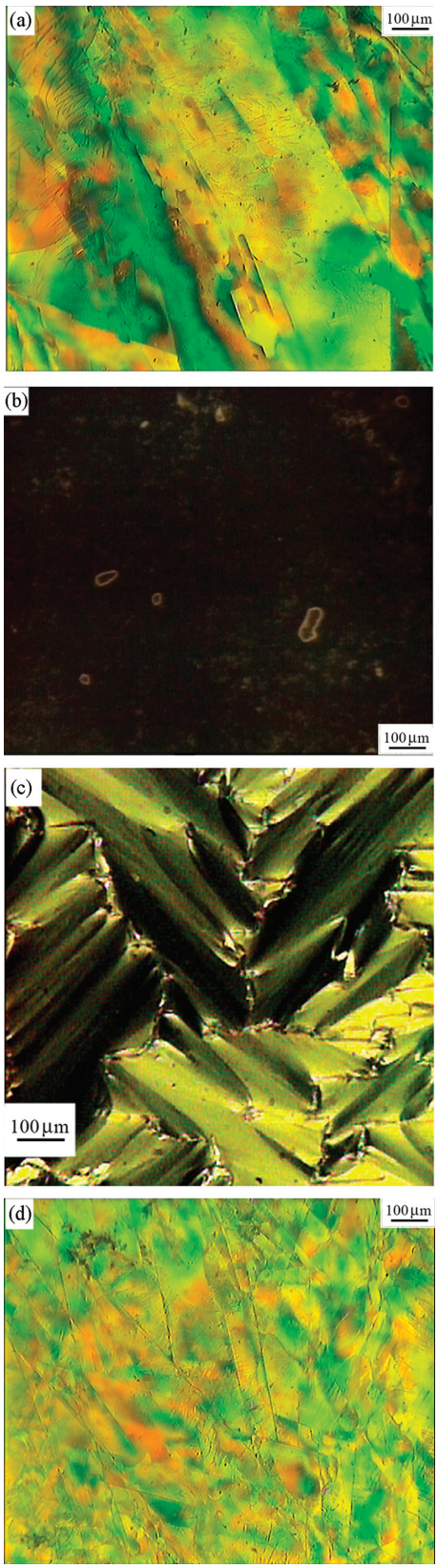

FIG. 4. (Color online) LC textures in unidirectionally oriented LC cells: (a) C_G phase of SWCNT-7OBA in a 8-μm-thick cell ($c = 0.01$ wt %) at $T = 87\,^\circ$C; (b) the nematic phase of pristine 7OBA for comparison; (c) the smectic-C phase of pristine 7OBA for comparison; (d) C_G phase of SWCNT-7OBA in a 20-μm-thick cell ($c = 0.007$ wt %) at $T = 87\,^\circ$C.

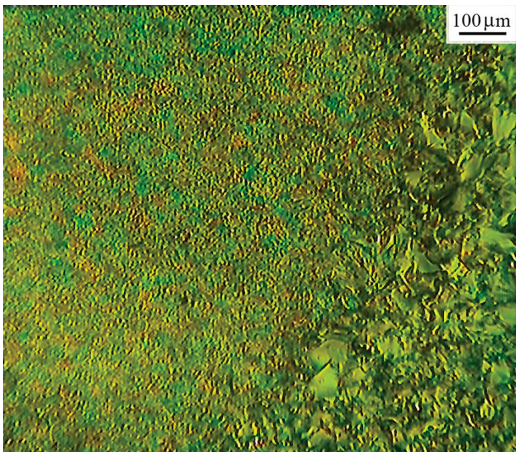

FIG. 5. (Color online) Competition of the S_C and the $S_C{}^*$ phase of SWCNT-7OBA in a nanocomposite with $c = 0.007$ wt % in a nonoriented LC cell with $d = 20$ μm at about 90 °C.

For $d = 8$ μm and $c = 0.01$ wt %, again the same chiral-phase sequence occurs down to the smectic-C_G whose texture is shown in Fig. 4(a). For comparison, we present the corresponding images of pristine 7OBA obtained for the same layer thickness from its conventional N phase [Fig. 4(b)] and its well oriented achiral S_C phase [Fig. 4(c)].

In addition, we checked the phase development at $c = 0.007$ and 0.004 wt % for $d = 20$ μm in both oriented and nonoriented LC cells. In the oriented cell we observed the same sequence of phase transitions for the chiral phases N^*, $S_C{}^*$, $N_r{}^*$, and C_G. The C_G texture for $c = 0.007$ wt % is shown in Fig. 4(d). The same textures were observed also for $c = 0.004$ wt %. The larger unicolored areas in Fig. 4(a) as compared to Fig. 4(d) reflect formation of larger single-crystalline domains in the thinner-layer texture due to the stronger surface influence. In the nonoriented cell we observed a fluctuation of growing achiral S_C and a competition of this phase with the chiral $S_C{}^*$ as depicted in Fig. 5.

3. Discussion

Table I summarizes the LC phases induced in SWCNT-7OBA, the most favorable conditions for their establishment, and the corresponding phase transition temperatures. It is noteworthy that in the nanocomposite, the $N \rightarrow S_C$ transition temperature (98 °C in pristine 7OBA) is lowered by 3.5 °C on average, and the 7OBA-specific S_C temperature region is divided into two regions where the S_C ($S_C{}^*$) and the N_r ($N_r{}^*$) phases appear, respectively. As a smectic-G phase is established below the reentrant nematic state, if the latter is additionally a chiral state, the subsequent G phase is also chiral, i.e., it is a C_G phase.

We establish symmetry changes in the system provoked by a combination of two effects—bulk-type influence from thermal activation and SWCNT-LC interaction, and surface-type influence from the cell plate, the latter being further enhanced for oriented plates. Reducing the cell thickness increases the anchoring energy and imposing unidirectional surface alignment lowers the symmetry similarly to the case when an external pressure is applied on the system. This effect creates favorable conditions rather for transitions to chiral phases instead of achiral ones. The $S_C{}^*$ then displays all textural characteristics of the helielectric C^* phase. Locally C^* has a C_2 symmetry with its spontaneous-polarization vector $\boldsymbol{P}$ lying in the plane of the layers, but because it is chiral (has a hand), it has globally D_∞ symmetry. Besides, when conventional achiral S_C is frustrated, the subsequent $S_C{}^* \rightarrow N_r{}^*$ transition indicates destruction of the smectic-C fluctuation (weak time and space correlation of the dimer molecules) and loss of the possibility for a formation of a stable achiral smectic-C layer with stable tilt angle. The reentrant nematics also indicates that at these surface and temperature conditions monomers and open dimers dominate in the LC system and suppress the smectic layering, thus leading to a return of the long-range positional order typical for N phases. At further cooling, however, the bent dimers gain dominance and restoration of the smectic layering then leads to a fluid tilted smectic-C_G state (without positional order inside the layers).

TABLE I. Optimal conditions for development of LC states induced in the nanocomposite SWCNT-7OBA with the corresponding phase transition temperatures. For simplicity, the two close-by lying transitions $I \rightarrow N$ and $N \rightarrow N^*$ are presented as one $I \rightarrow N^*$ transition.

LC cell	c (wt %)	$T(I \rightarrow N)$ (°C)	$T(N \rightarrow S_C)$ (°C)	$T(S_C \rightarrow N_r)$ (°C)	$T(N_r \rightarrow G)$ (°C)	$T(G \rightarrow \text{Cry})$ (°C)
Nonoriented $d = 20$ μm	0.01	142	93	86	81	75
LC cell	c (wt %)	$T(I \rightarrow N^*)$ (°C)	$T(N^* \rightarrow S_C{}^*)$ (°C)	$T(S_C{}^* \rightarrow N_r{}^*)$ (°C)	$T(N_r{}^* \rightarrow C_G)$ (°C)	$T(C_G \rightarrow \text{Cry})$ (°C)
Nonoriented $d = 8$ μm	0.01	142	93	90	86	75
Oriented d=20 μm	0.01	142	95	92.5	89	70
Oriented $d = 8$ μm	0.01	142	94	93	88	72
Nonoriented $d = 20$ μm	0.007	142	95.5	89.5	88	80
Oriented $d = 20$ μm	0.007	142	95	92	89	60

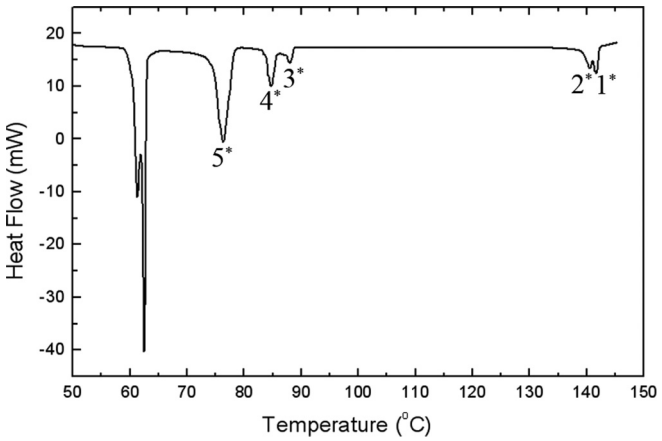

FIG. 6. DSC exo scan (cooling rate 2 °C min^{-1}) of the nanocomposite (c = 0.01 wt %). The symbols 1*,2*,3*,4*, and 5* mark the peaks corresponding to the five induced transitions $I \rightarrow N$, $N \rightarrow N^*$, $S_C{}^* \rightarrow N_r{}^*$, $N_r{}^* \rightarrow C_G$, and $C_G \rightarrow$Cry from the isotropic down to the solid crystal state.

B. DSC results

The thermal parameters of these induced phases in the SWCNT-7OBA nanocomposite were additionally examined by DSC analysis. The corresponding scan in its exo recording is presented in Fig. 6. For comparison, we present in Fig. 7(a) a reference DSC scan of a pristine-7OBA sample, where these phases do not appear. For both SWCNT-7OBA and pristine 7OBA we used sample weights between 4 and 6 mg. This choice was a compromise between the necessity to minimize the thermal-conduction-induced delay and the need to maintain a good signal-to-noise ratio.

The phase transition temperatures and the corresponding enthalpies ΔH for SWCNT-7OBA (c = 0.01 wt %) and pristine-7OBA samples are reported in Table II. Figures 7 and 8 demonstrate that instead of the three typical peaks, 1, 2, and 3, of pristine 7OBA displaying the transitions $I \rightarrow N$, $N \rightarrow S_C$, and $S_C \rightarrow$Cry, respectively, SWCNT-7OBA exhibits five peaks, 1*,2*,3*,4*, and 5*, displaying the corresponding transitions $I \rightarrow N$, $N \rightarrow N^*$, $S_C{}^* \rightarrow N_r{}^*$, $N_r{}^* \rightarrow C_G$, and $C_G \rightarrow$Cry. A comparison of Table II with Table I yields a good agreement of the DSC data with the transition temperatures determined by our microtexture analysis for the nonoriented SWCNT-7OBA sample with d = 8 μm. The DSC scanning did not detect a peak corresponding to the $N^* \rightarrow S_C{}^*$ transition, probably due to its second-order character. On the other hand, the enthalpies of the transitions $I \rightarrow N$, $N \rightarrow N^*$, $S_C{}^* \rightarrow N_r{}^*$, $N_r{}^* \rightarrow C_G$, and $C_G \rightarrow$Cry quoted in Table II unambiguously indicate their first-order character. The two intense peaks below the $C_G \rightarrow$Cry and $S_C \rightarrow$Cry transition in Figs. 6 and 7, respectively, depict transitions between different solid crystal states characteristic for H-bonded LC systems.

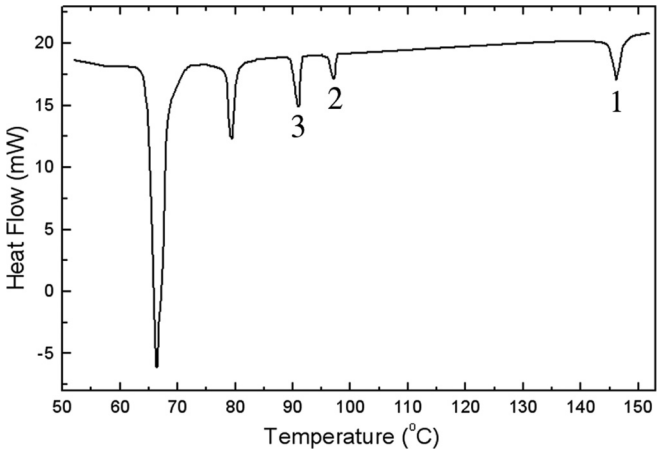

FIG. 7. DSC exo scan (cooling rate 2 °C min^{-1}) of pristine 7OBA. The symbols 1, 2, and 3 mark the peaks corresponding to the well known phase transitions $I \rightarrow N$, $N \rightarrow S_C$, and $S_C \rightarrow$Cry, respectively.

TABLE II. Transition temperatures and enthalpies as determined by DSC for the phase transitions detected in the SWCNT-7OBA nanocomposite (SWCNT concentration of 0.01 wt %). The corresponding data for pristine 7OBA are also quoted for comparison.

c (0.01 wt %)		7OBA	
T (°C)	ΔH (kJ/mol)	T (°C)	ΔH (kJ/mol)
$T(I \rightarrow N) = 143$	2.51	$T(I \rightarrow N) = 146$	2.51
$T(N \rightarrow N^*) = 142$	2.72	$T(N \rightarrow S_C) = 97$	10.88
$T(S_C{}^* \rightarrow N_r{}^*) = 90$	0.42	$T(S_C \rightarrow \text{Cry}) = 91$	19.25
$T(N_r{}^* \rightarrow C_G) = 86$	1.65		
$T(C_G \rightarrow \text{Cry}) = 77$	10.23		

C. Raman spectroscopy

To check the results from the microtexture analysis we performed also a comparative monitoring of the different

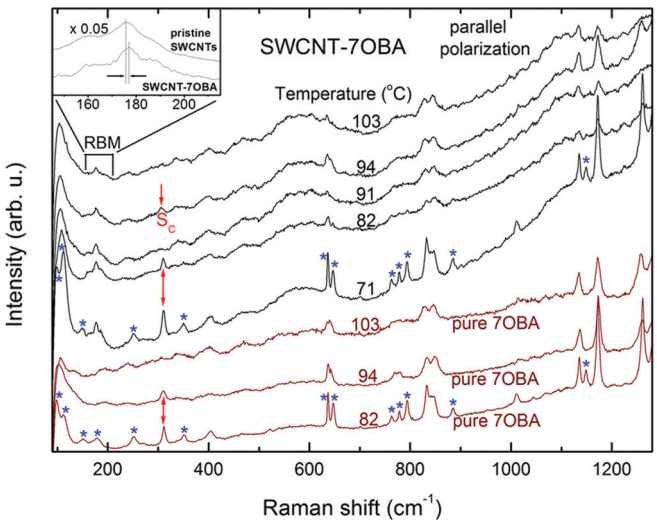

FIG. 8. (Color online) Raman spectra of SWCNT-7OBA in parallel polarization at several temperatures (quoted in the plot) in the low-frequency region (100–1300 cm^{-1}). The lowest three traces are spectra of pristine 7OBA for comparison. The peak at 310 cm^{-1} appearing in the S_C phase is marked by arrows and the symbol S_C. The sharp peaks emerging upon transition to the Cry state are marked with asterisks. The inset shows at an expanded scale the RBM region of the SWCNT-7OBA spectrum at 82 °C and a spectrum of pristine SWCNTs heated to 82 °C before mixing to the LC.

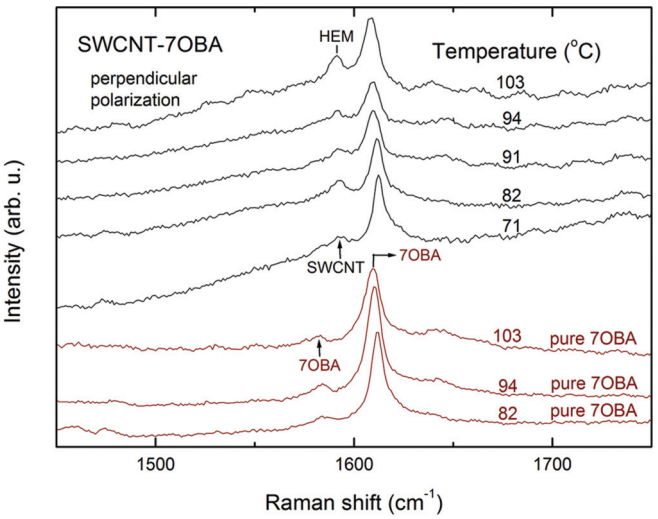

FIG. 9. (Color online) Raman spectra of SWCNT-7OBA at several temperatures (quoted in the plot) in the high-frequency region (1450–1750 cm^{-1}). The lowest three traces are spectra of pristine 7OBA for comparison. Two LC peaks neighboring the HEM band are marked with 7OBA and the spectra are recorded in perpendicular polarization of incident and scattered light in order to facilitate distinguishing of the HEM band at 1592 cm^{-1} from the intense 7OBA peak at ≈1610 cm^{-1}.

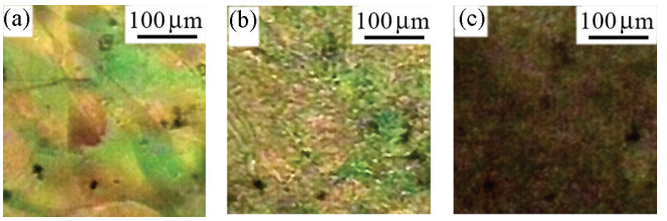

FIG. 10. (Color online) C_G textures of SWCNT-7OBA illustrating the bistability at dc electric field applied on a nanocomposite cell for $c = 0.01$ wt % and $d = 20$ μm. (a) The nonexcited state without electric field; (b) same texture after applying a field of 0.59 V/μm; (c) same texture upon reversal of the field polarity.

phases of SWCNT-7OBA (oriented LC cell with $d = 8$ μm and $c = 0.01$ wt %) and pure 7OBA with Raman spectroscopy. The resulting spectra are displayed in Figs. 8 and 9 for low- and high-frequency vibrations, respectively. With the radial breathing mode (RBM) centered at about 177 cm^{-1} and the bond-stretching high-energy mode (HEM) at ≈1592 cm^{-1} the signature of carbon nanotubes is clearly visible in the spectra of SWCNT-7OBA, confirming the presence of small SWCNT bundles in the nanocomposite. Except for the RBM and the HEM band, no essential differences between SWCNT-7OBA and pure 7OBA are found in their Raman spectra from the I phase down to 100 °C, but upon further cooling a number of significant changes occur.

Along with the $N \rightarrow S_C$ transition in pure 7OBA, a specific peak appears at 310 cm^{-1} as evident from the spectrum at 94 °C (see Fig. 8). This peak can serve as a distinguishing feature of the S_C phase in 7OBA as it represents the only difference in the Raman spectra of this substance between the N and the S_C phase. The transition to a solid phase causes remarkable further changes, as can be seen from the lowest spectrum in Fig. 8 taken at 82 °C: Additional peaks appear at 150, 178, 252, 351, 885, and 1148 cm^{-1}; the bands at 105 and 638 cm^{-1} split into two and that at 777 cm^{-1} into three sharp peaks.

We now analyze the Raman spectra of the SWCNT-7OBA nanocomposite starting with the $N^* \rightarrow S_C*$ transition expected at 94 °C (see Table I). The corresponding spectrum for 94 °C in Fig. 8 indeed contains the peak at ≈310 cm^{-1} identifying the smectic phase although this peak is slightly softened and broader compared to that of pure 7OBA. In the next spectrum taken at 91 °C this peak is absent which is consistent with the reentrant nematic phase from 93 °C to 88 °C established by the microtexture analysis. The next spectrum measured at 82 °C contains again a sharp and relatively intense peak at 310 cm^{-1} and resembles in its structure the pure-7OBA spectrum at 94 °C suggesting that the behavior of this C_G phase in Raman scattering is similar to that of the conventional S_C phase. Finally, the spectrum taken at 71 °C closely resembles the pure-7OBA spectrum at 82 °C with all additional sharp peaks indicating solidification of the nanocomposite. The Raman spectra of SWCNT-7OBA are thus consistent with the sequence of phase transitions found by microtexture analysis (see Table I) in this nanocomposite.

The richer phase development in SWCNT-7OBA is undoubtedly connected to an interaction of the LC molecules with the nanotubes and it would be interesting to find evidence for this interaction in the Raman spectra. Such interaction in form of strong intermolecular overlap of π orbitals (π stacking) was reported for SWCNTs mixed into the liquid crystal 5CB [36]. Evidence for this π stacking was found in the established slight hardening of the RBM band of these SWCNTs [36]. The RBM band with vibrational pattern perpendicular to the nanotube-bundle axis can serve as a sensitive probe for interactions of SWCNTs with molecules in contact with their surface, as well as for interactions among the SWCNTs themselves, e.g., within a bundle [37]. As the 7OBA molecule also contains phenyl rings, it is logical to expect its interaction with the SWCNTs to be reflected in the behavior of the RBM band of SWCNT-7OBA. We compared Raman spectra of the pristine-SWCNT powder before mixing it into the liquid crystal with spectra of the SWCNT-7OBA nanocomposite and found indeed a slight RBM hardening and redistribution of its intensity in the SWCNT-7OBA spectra. This comparison is depicted for the C_G phase in the inset of Fig. 8 for $T = 82$ °C. The RBM band of the SWCNTs used in the present study consists of three features: a main peak and two shoulders on both sides. For the pristine tubes their frequencies were determined as follows: 159.5, 176, and 188 cm^{-1}. In the SWCNT-7OBA spectra the low-energy shoulder hardens by 3 cm^{-1}, the main RBM peak by 1 cm^{-1}, and the high-energy shoulder also by 1 cm^{-1} with simultaneous transfer of spectral weight from the low-energy to the high-energy shoulder. We consider this clear evidence for interaction of the LC molecules with the nanotubes and regard this interaction as the factor breaking the one H bond in the central hexagon and leading to a bent-dimer shape of the 7OBA molecules in the nanocomposite.

D. Microtexture analysis with application of electric field

The best way to confirm C_G and to distinguish it from other chiral phases (e.g., C^*) is certainly the demonstration of its specific electro-optical behavior. The bent-dimer form of the 7OBA molecule is polar and therefore, the C_G phase should possess a net permanent polarization, while C^* is not typically ferroelectric [27,28,30–33].

The best large chiral C_G domains were grown in cells with thickness of 8 and 20 μm, but in order to avoid short circuiting, we had to use thicker cells. To obtain well observable electro-optical effects, we generally used cell thicknesses of 50 μm (unless specified otherwise) although the obtained C_G textures consisted of smaller grainlike domains due to the weakened surface influence in thicker cells. Varying the parameters of the applied field, the temperature, and the cooling rate, we observed various electro-optical effects typical for the C_G phase in its bent-core molecule manifestation.

The existence of a permanent polarization $\boldsymbol{P}$ in the C_G phase of SWCNT-7OBA can be demonstrated with a dc electric field applied along the LC cell normal (up view configuration). We observe the following two effects:

(i) Applying a dc electric field of at least 0.59 V/μm on a cell with $d = 20$ μm leads to a reorientation of the LC director, which is visualized as a transition from a typical normal-state texture [state a depicted in Fig. 6(a)] to an excited state b shown in Fig. 10(b). Upon reversing the field polarity the system switches to another significantly darker-colored state c shown in Fig. 10(c). The excited states b and c exhibit a strong memory effect by remaining unchanged on the minute scale after switching off the field. Further reversing the field polarity leads only to switching between the states b and c, i.e., between light and dark appearance of the texture. This switching is also accompanied by color change from green (stronger birefringence, state b) to pink (weaker birefringence, state c). The director orientation can thus be changed in a bistable way with a dc electric field of at least 0.59 V/μm. This threshold-field effect emphasizes the difference from C^*, where a similar electro-optical response [29] occurs without a threshold field since in this phase the allowed director orientation is infinitely degenerate on the tilt-angle cone. The observed threshold behavior in our SWCNT-7OBA nanocomposite indicates that the bent-dimer adopts only a discrete set of orientations on the tilt-angle cone similarly to that of bent-core molecules in C_G phase [31–33].

(ii) Rapid cooling at 3 °C/min from the I phase in a dc field of 0.23 V/μm creates circularlike domains [see Fig. 11(a)] among a grainy nonspecific texture in the C_G phase. Upon increasing the field magnitude from zero to 0.5 V/μm at constant temperature, the color indicating the birefringence magnitude in the surrounding grain domains changes continuously and reversibly from green through pink (red) until finally a light yellow color establishes [Fig. 11(b)]. Due to the already mentioned memory effect this picture persists even after the field is switched off. On the other hand, the texture changes dramatically if a stronger field of at least 0.58 V/μm is applied. Thick ropelike filaments appear around the circularlike domains parallel to the layers [Fig 11(c)] and also remain unchanged after the field removal. Bistable switching between the textures in Figs. 11(a) and 11(c) is observed upon alternating the field polarity at magnitudes over the threshold similarly to case (i).

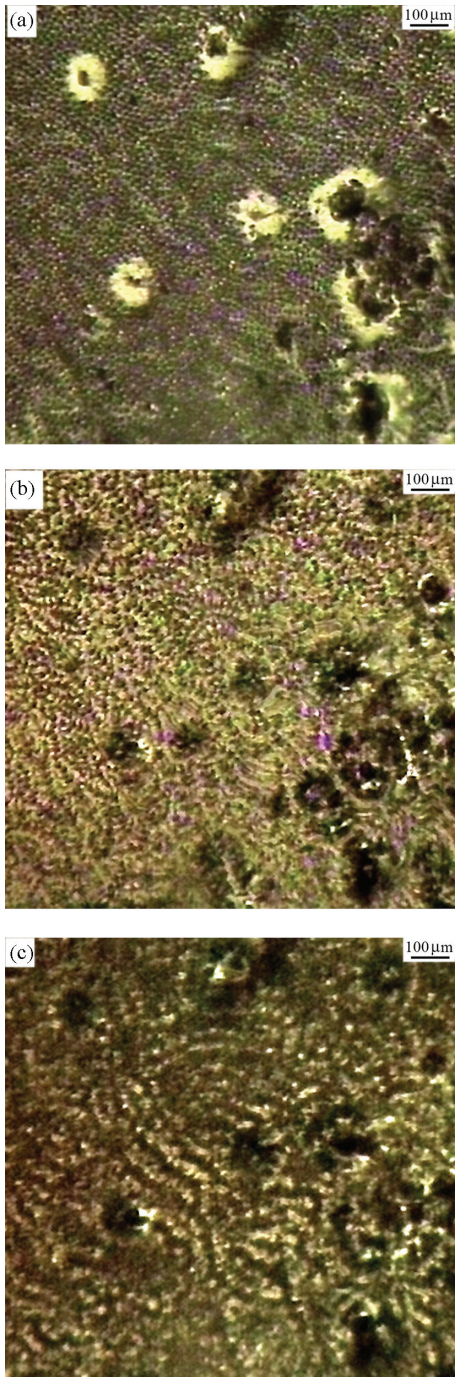

FIG. 11. (Color online) C_G texture of SWCNT-7OBA for $c =$ 0.01 wt % and $d = 50$ μm after rapid cooling at 3°C/min from the I phase in the presence of a dc field of 0.23 V/μm. (a) Circularlike domains among a grainy nonspecific texture; (b) the surrounding grain domains after increasing the field magnitude from zero to 0.5 V/μm, in the course of continuous change in birefringence color from green to yellow; (c) same texture at 0.58 V/μm containing thick ropelike filaments around the circularlike domains.

In Fig. 12 the probable mechanism of the observed bistabilities in cases (i) and (ii) is schematically depicted.

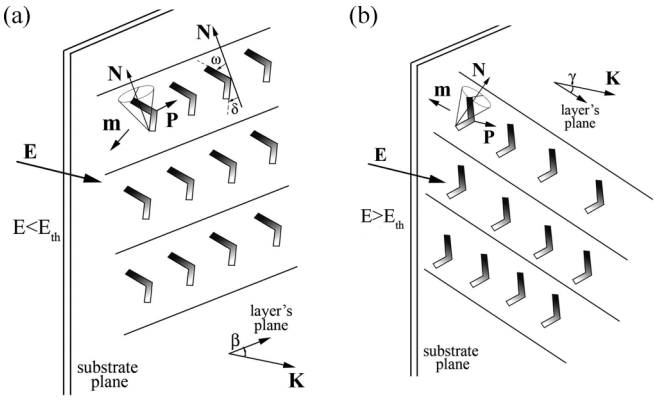

FIG. 12. A scheme of the bistability of the C_G texture at dc field. (a) Without electric field $\boldsymbol{E}$ or at fields below the threshold the layer's planes within one domain are initially tilted at angle β to the substrate normal $\boldsymbol{K}$. The kink vector $\boldsymbol{m}$, the clinic angle ω, and the leaning angle δ are also indicated. (b) An electric field surpassing the threshold causes the layers to tilt additionally to align $\boldsymbol{P}$ parallel to it, reaching another angle, γ to the substrate normal $\boldsymbol{K}$ and forming another discrete chevron alignment.

Without electric field, domains of different birefringence contain layers tilted at different angles to the substrate normal thus forming the so-called discrete chevron configuration [29]. Let us assume that the layer's planes within one domain are initially tilted at angle β to the substrate normal $\boldsymbol{K}$ [Fig. 12(a)]. Applying electric field $\boldsymbol{E}$ below the threshold along the substrate normal $\boldsymbol{K}$ causes only a rotation of the director on the tilt-angle cone and no field-induced change in the textures is observed. If the field magnitude surpasses the threshold, energy minimization causes the layers, which are strongly coupled via the out-of-layer-plane polarization component, to tilt accordingly to align $\boldsymbol{P}$ parallel to $\boldsymbol{E}$, reaching another angle, γ, to the substrate normal $\boldsymbol{K}$ [see Fig. 12(b)], and forming another discrete chevron alignment. Bistable switching by sufficiently strong electric field should then be possible between both chevron alignments defined by the angles β and γ as indeed observed.

The complexity of the electro-optical response of C_G can be demonstrated by means of ac electric field. Depending on the experimental conditions, during the nucleation of C_G, ropelike as well as large chiral domains grow simultaneously. The ropelike domains transform in grainy texture, whereas the large chiral domains remain unchanged or transform in ribbonlike ones upon slow (0.1 °C/min) cooling within the C_G phase. It seems that both domain types have the same origin – chirality in the smectic layers. Obviously, the nucleation energy of both types of chiral domains is similar so that they can coexist. Applying low-frequency ac field (<10 Hz, 0.1 V/μm) on a 50-μm-thick cell, one observes that some low-birefringence ribbonlike domains stable at constant temperature [see Fig. 13(a)] shrink or broaden depending on the polarity, and for a given polarity shrinking and broadening domains can coexist. Furthermore, the shrinking causes a coiling of the one ribbon end. At some places we observed ropelike domains [shown in Fig. 13(b)] that only shrank upon polarity alternation. The coexistence of such ribbon- and ropelike domains with different birefringence shows close resemblance to the B_7 phase in bent-core molecules and suggests that C_G is really analog to this phase [38]. The electric field causes the ribbons in some places to coalesce in regular stripes with width smaller than the cell thickness. This effect is thresholdless and shows that the ribbons are polar and that the vector $\boldsymbol{P}$ has a component parallel to the substrate surface. Application of electric field $\boldsymbol{E}$ produces a torque $\boldsymbol{M} \sim \boldsymbol{m} \times \boldsymbol{E}$ on the ribbonlike domains. We assume this torque to cause the mentioned coiling of the one ribbon end [shown in Fig. 13(c)] which is right- or left-handed depending on the direction of $\boldsymbol{E}$. Coiling of ribbons is another way to compensate their polarization in order to satisfy the condition div$\boldsymbol{P}$ = 0. The difference in the behavior of ribbonlike and ropelike domains shows that the twist deformation typical for chiral systems is occasionally replaced by the coil formation since a helical shape has less elastic energy than the corresponding twisted form. In any case, the behavior of both domain kinds in electric field implies a nonzero $\boldsymbol{P}$ component perpendicular to the layers.

It is important to point out that the electro-optical effects described above occur in a restricted temperature interval within the C_G range. At its lowest temperature we observed enhancement of the green coloring indicating large birefringence and hence prevailing quasiplanar anchoring, while near the upper temperature limit the birefringence decreases resembling that in enhanced quasihomeotropic configuration. Application of electric field in these terminal cases does not induce any electro-optical effects. The onset of electro-optical response is detected at 0.2 °C below the $N_r^* \rightarrow C_G$ transition indicating the onset of coupling to the field of an emerging out-of-layer polarization and all electro-optical effects disappear again at 0.4 °C above the solidification threshold where the

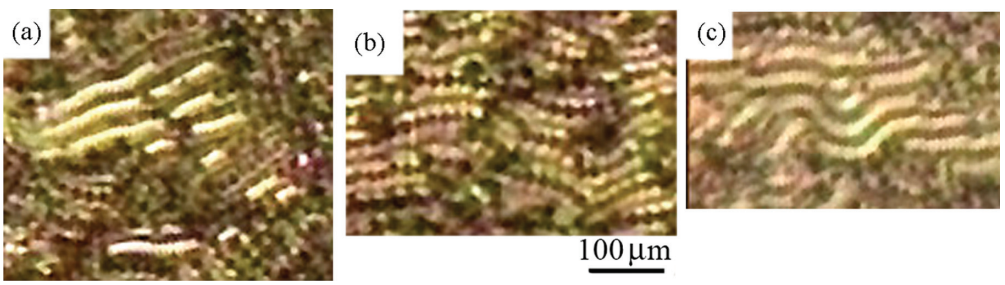

FIG. 13. (Color online) Response of C_G texture of SWCNT-7OBA for $c = 0.01$ wt % and $d = 50$ μm to ac field of 0.1 V/μm (<10 Hz): (a) Low-birefringence ribbonlike domains with approximate width of 50 μm, shrinking or broadening depending on the polarity; (b) ropelike domains which only shrink upon polarity alternation; (c) ribbons twisting into right- or left-handed spirals depending on the polarity.

out-of-layer polarization component possibly vanishes again. Furthermore, no such C_G-specific electro-optical response was detected in any other phase above the C_G range up to the isotropic state, nor in any phase of pristine 7OBA. This clearly shows that only the C_G phase exhibits macroscopic spontaneous polarization having both a component parallel to the layers as well as a component perpendicular to the layers. Since a moderate electric field cannot change the tilt angle, we conclude that the C_G phase arises from the decoupling of the leaning angle from the clinic one through the variation of the leaning angle with temperature [33]. The position of a distinct 7OBA molecule with its clinic angle ω and leaning angle δ in a C_G layer is shown in Fig. 12(a). A transition from C^* to C_G seems to be possible due to the temperature dependence of the leaning angle.

It is known that the patterns formed at phase transition require div$\boldsymbol{P} = 0$ [29]. To satisfy this requirement in C_G, however, a compensation of the divergence of the out-of-layer polarization ($\boldsymbol{P}_{\rm out}$) is needed. Such compensation leads to additional deformation (coiling up) of the rope- and ribbonlike texture domains, as shown in Fig 13(c) for the ribbonlike domains. Since the ropelike textures exhibit some initial coiling, they do not show any response to an electric field $\boldsymbol{E}$. In uniformly shrinking domains (ribbons) div$\boldsymbol{P}_{\rm out}$ is not zero, and the free energy depends on the field polarity. Following [19,26],when $\boldsymbol{E}$ is opposite to $\boldsymbol{P}_{\rm out}$ the free energy increases by $\boldsymbol{P}_{\rm out}\cdot\boldsymbol{E}$ inducing a transition from C_G to above-lying phases up to the I state. Especially, for an electric field of at least 0.4 V/μm we observe such a transition between C_G and C^* (displayed in Fig. 14). We thus have electric-field-induced phase transition governed by temperature-dependent threshold field. In other words, we observe an equivalent decrease of the phase transition temperature driven by the electric field [39]. On the other hand, a stronger field of any polarity could promote a transformation of the texture into an achiral smectic-C [see Fig. 1(b), lower part] by passing through C^*.

Using the ferroelectrically induced decrease ΔT of the phase transition temperature, we can assess the polarization by the modified Kirkwood-Helfrich equation [29,30,39]:

$$(\Delta T/T_{\rm o})(\Delta H/M_\rho) = 0.5\varepsilon_{\rm a}\varepsilon_0|\boldsymbol{E}|^2 - |\boldsymbol{P}||\boldsymbol{E}|\cos\phi,$$

where $T_{\rm o}$ is the $C_G \rightarrow C^*$ transition temperature at $\boldsymbol{E} = \boldsymbol{0}$, M is the molar mass, ρ the density of the nanocomposite, and ϕ is the angle between $\boldsymbol{P}$ and $\boldsymbol{E}$. We have observed these effects for dc and ac fields of very low frequencies ($\leqslant$10 Hz), where the coupling to $\boldsymbol{P}$ dominates and the quadratic term with $\varepsilon_{\rm a}$ can be neglected compared to the contribution of $\boldsymbol{P}$. We use the following numerical values: $T_{\rm o} = 362$ K, $M = 10^3$ kg, $\rho = 10^3$ kg m^{-3}, $\Delta H = 1.65$ kJ mol^{-1}, and $|\boldsymbol{E}| = 0.36 \times 10^6$ V/m. Applying an electric field of magnitude 0.4 V/μm with frequency $\leqslant$10 Hz creates low-birefringent domains in the same way as does heating by $\Delta T \approx 2\,^\circ$C without a field. Thus we estimate that $|\boldsymbol{P}_{\rm out}| \approx 110$ nC/cm^2. This value obtained in a pyroelectric approach is consistent with the polarization magnitudes obtained for the bent-core molecular LC systems [30,40]

We also employed the triangular wave technique to measure the spontaneous polarization $\boldsymbol{P}$ in an alternative way [29,33,41,42]. The triangular waves were generated by a function generator (for $U = 30$ V with frequency of 40 Hz) and we determined $|\boldsymbol{P}_{\rm out}| \approx 113$ nC/cm^2. This value compares well with that obtained by the above-presented pyroelectric method with a difference between them of only $\approx$3%.

Finally, we focus on the symmetry properties of the smectic-C_G phase [Figs. 2(c), 3(c), 4(a), and 4(d)] where the subscript G stands for general. The anisotropic in-plane fluidity of C_G (like that of achiral S_C) requires that none of the principle axes of the second rank tensor [27,28], characterizing the orientational order, makes an angle of 0° or 90° with the smectic layer's planes. So the smectic-C_G type observed here is a chiral phase, formed due to a symmetry lowering in each distinct 7OBA molecule and we assume this to occur by adopting the bent-dimer shape. The necessary energy for this slight deformation can only come from an interaction with the SWCNTs which represent the only difference between pristine 7OBA and the nanocomposite. The SWCNTs thus impose a chirality-inducing bulk impact on the LC host matrix as was found recently for other achiral nematics [20]. From the Raman spectra of the nanocomposite we indeed have evidence for such interaction of the π-stacking type causing a slight upshift of the RBM band of SWCNTs in the nanocomposite.

In addition to the fluidity, chirality, and the biaxial structure of the C_G phase established by microtexture analysis, our electric-field experiments provide evidence for a permanent macroscopic polarization with a nonvanishing out-of-layer component thus confirming the triclinic C_1 symmetry of this phase. Therefore, besides bulk ferroelectricity, it should reveal both left-handed and right-handed versions. This provides a natural explanation for the equal number of left- and right-handed helices, which we observe by microtexture analysis.

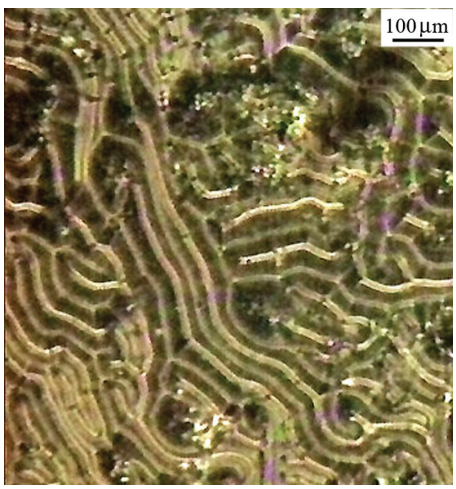

FIG. 14. (Color online) A C^* texture of SWCNT-7OBA obtained through a transition from C_G at a dc field of 0.4 V/μm.

IV. CONCLUSION

In the nanocomposite SWCNT-7OBA we find a variety of phase transitions and corresponding phases, which are different with respect to those observed in pristine 7OBA as well as shifts in the temperatures of known transitions. In general, this effect is due to the molecular structure of hydrogen-bonded

7OBA and especially to its basic structure element—the dimer ring. From a series of investigated mixtures we establish SWCNT concentrations in the range 0.004 wt %–0.01 wt % to be appropriate for achieving sufficient conformability between both materials, necessary for the induction of these liquid crystal (LC) states. We conclude that the LC cell surface orientation and the bulk interaction of the 7OBA molecules with the SWCNTs can cause a transformation of the dimer rings, which is equivalent to lowering the symmetry of the LC system. These two factors are thus of primary importance for the type of LC states obtained in the nanocomposites. An important result is that some of these induced states are chiral, whereas 7OBA is achiral in its pristine state. Comparative examination of the nanocomposite and pristine 7OBA with temperature-dependent Raman spectroscopy and differential scanning calorimetry corroborates the existence of these phases and phase transitions in SWCNT-7OBA. Our Raman results also provide additional confirmation for the presence of SWCNTs in the nanocomposite and for their interaction with the 7OBA molecules.

We observe a reentrant nematic below an achiral smectic-*C* phase and a reentrant chiral nematic below a chiral smectic-*C* phase in the SWCNT-7OBA nanocomposite, indicating a depressing of the smectic-*C* layering (favored by closed dimers) and a rebuilding of the nematic long-range order. We also demonstrate that below the chiral reentrant nematic state the bent-dimer domination produces a triclinic tilted smectic-C_G phase. We provide a full characterization of this phase showing it to be chiral, biaxial, and to exhibit anisotropic in-layer fluidity. The detected electro-optical properties of this phase confirm that it possesses a permanent polarization in a direction oblique to the layers. In combination with the established helical properties, this confirms that the C_G phase is ferroelectric in the bulk. The performed electric-field experiments also reveal several bistabilities with low-threshold fields and enable us to numerically estimate the spontaneous-polarization magnitude in the C_G phase of the SWCNT-7OBA nanocomposite, which is consistent with the corresponding values obtained for bent-core molecular LC systems.

ACKNOWLEDGMENTS

This study was supported by Grant No. BK-2/11 from the Institute of Solid State Physics, Bulgarian Academy of Sciences. The Korean Ministry of Education, Science and Technology is acknowledged for support from the World Class University Project (WCU, Grant No. R32-2008-000-10082-0).

[1] I. Dierking, G. Scalia, and P. Morales, J. Appl. Phys. **97**, 044309 (2005).
[2] J. M. Russel, S. Oh, I. LaRue, O. Zhou, and E. T. Samulski, Thin Solid Films **509**, 53 (2006).
[3] M. D. Lynch and D. L. Patrick, Nano Lett. **2**, 1197 (2002).
[4] I. Dierking, G. Scalia, P. Morales, and D. LeClere, Adv. Mater. **16**, 865 (2004).
[5] R. Basu and G. Iannacchione, Appl. Phys. Lett. **93**, 183105 (2008).
[6] I.-S. Baik, S. Y. Jeon, S. H. Lee, K. A. Park, S. H. Jeong, K. H. An, and Y. H. Lee, Appl. Phys. Lett. **87**, 263110 (2005).
[7] J. P. F. Lagerwall and G. Scalia, J. Mater. Chem. **18**, 2890 (2008).
[8] R. Basu and G. S. Iannacchione, Phys. Rev. E **80**, 010701 (2009).
[9] K.-J. Wu, K.-C. Chu, C.-Y. Chao, Y.-F. Chen, C.-W. Lai, C.-C. Kang, C.-Y. Chen, and P.-T. Chou, Nano Lett. **7**, 1908 (2007).
[10] Q. Liu, Y. Cui, D. Gardiner, X. Li, S. He, and I. I. Smalyukh, Nano Lett. **10**, 1347 (2010).
[11] C. Zamora-Ledezma, C. Blanc, N. Puech, M. Maugey, C. Zakri, E. Anglaret, and P. Poulin, Phys. Rev. E **84**, 062701 (2011).
[12] S. Y. Jeon, S. H. Lee, and Y. H. Lee, Appl. Phys. Lett. **89**, 056102 (2006).
[13] H. Gommans, J. W. Alldredge, H. Tashiro, J. Park, J. Magnuson, and A. G. Rinzler, J. Appl. Phys. **88**, 2509 (2000).
[14] F. Podgornov, A. Suvorova, A. Lapanik, and W. Haase, Chem. Phys. Lett. **479**, 206 (2009).
[15] K. Park, S. Mi Lee, S. H. Lee, and Y. H. Lee, J. Phys. Chem. C **111**, 1620 (2007).
[16] R. Basu, R. G. Petschek, and C. Rosenblatt, Phys. Rev. E **83**, 041707 (2011).
[17] P. Malik, A. Chadhary, R. Mehra, and K. K. Raina, J. Mol. Liq. **165**, 7 (2012).
[18] R. Basu, K. Boccuzzi, S. Ferjani, and C. Rosenblatt, Appl. Phys. Lett. **97**, 121908 (2010).
[19] R. Basu and G. S. Iannacchione, Phys. Rev. E **81**, 051705 (2010).
[20] R. Basu, C.-L. Chen, and C. Rosenblatt, J. Appl. Phys. **109**, 083518 (2011).
[21] S. Ghosh, A. K. Sood, and N. Kumar, Science **299**, 1042 (2003).
[22] P. A. Kumar, V. G. K. M. Pisipati, A. V. Rajeswary, and S. Sreehary Sastry, Z. Naturforsch. A **57**, 184 (2002).
[23] T. Niori, T. Sekine, J. Watanabe, T. Furukawa, and H. Takezoe, J. Mater. Chem. **6**, 1231 (1996).
[24] D. R. Link, G. Natale, R. Shao, J. E. Maclennan, N. A. Clark, E. Korblova, and D. M. Walba, Science **278**, 1924 (1997).
[25] D. A. Olson, A. Cady, W. Weissflog, H. T. Nguyen, and C. C. Huang, Phys. Rev. E **64**, 051713 (2001).
[26] P. J. Sebastiao, P. Simeao Carvalho, M. R. Chaves, H. T. Nguyen, and A. C. Ribeiro, Eur. Phys. J. E **20**, 55 (2006).
[27] H. R. Brand, P. E. Cladis, and H. Pleiner, Eur. Phys. J. B **6**, 347 (1998).
[28] P. E. Cladis, H. R. Brand, and H. Pleiner, Liquid Crystals Today **9**, 1 (1999).
[29] P. G. De Gennes and J. Prost, *The Physics of Liquid Crystals*, 2nd ed. (Oxford University Press, New York, 1993).
[30] A. Jakli, D. Kruerke, H. Sawade, and G. Heppke, Phys. Rev. Lett. **86**, 5715 (2001).
[31] N. Chattham, E. Korblova, R. Shao, D. M. Walba, J. E. Maclennan, and N. A. Clark, Phys. Rev. Lett. **104**, 067801 (2010).
[32] N. Chattham, E. Korblova, R. Shao, D. M. Walba, J. E. Maclennan, and N. A. Clark, Liq. Cryst. **36**, 1309 (2009).
[33] W.-H. Chen, W.-T. Chuang, U-S. Jeng, H.-S. Sheu, and H.-C. Lin, J. Am. Chem. Soc. **133**, 15674 (2011).
[34] D. M. Walba, E. Korblova, R. Shao, and N. A. Clark, J. Mater. Chem. **11**, 2743 (2001).

[35] M. Petrov, *Optical and Electrooptical Properties of Liquid Crystals Nematic and Smectic Phases* (Nova Science Publishers, New York, 2010).
[36] G. Scalia, J. Lagerwall, M. Haluska, U. Dettlaff-Weglikowska, F. Giesselmann, and S. Roth, Phys. Status Solidi B **243**, 3238 (2006).
[37] C. Thomsen, S. Reich, A. R. Goni, H. Jantoljak, P. M. Rafailov, I. Loa, K. Syassen, C. Journet, and P. Bernier, Phys. Status Solidi B **215**, 435 (1999).
[38] H. Pleiner, H. R. Brand, and P. E. Cladis, Ferroelectrics **243**, 291 (2000).
[39] W. Helfrich, Phys. Rev. Lett. **24**, 201 (1970).
[40] G. Heppke, D. D. Parhi, and H. Sawade, Ferroelectrics **243**, 269 (2000).
[41] K. Miyasato, Sh. Abe, H. Takezoe, A. Fukuda, and E. Kuze, Jpn. J. Appl. Phys. **22**, L661 (1983).
[42] V. M. Vaksman and Yu. P. Panarin, Mol. Mater. **1**, 147 (1992).